

**DIELECTRIC RELAXATION AND IMPEDANCE
SPECTROSCOPY OF NASICON TYPE
 $\text{Na}_{3+x}\text{Zr}_{2-x}\text{M}_x\text{Si}_2\text{PO}_{12}$ (M = DIVALENT, TRIVALENT,
TETRAVALENT ELEMENTS) OXIDES AND ION-
IRRADIATION EFFECTS**

**RAMCHARAN MEENA
(2019 PHZ 8034)**



**DEPARTMENT OF PHYSICS
INDIAN INSTITUTE OF TECHNOLOGY, DELHI
OCTOBER 2024**

© Indian Institute of Technology Delhi (IITD), New Delhi, 2024

**Dielectric relaxation and impedance spectroscopy of NASICON
type $\text{Na}_{3+x}\text{Zr}_{2-x}\text{M}_x\text{Si}_2\text{PO}_{12}$ ($M =$ divalent, trivalent, tetravalent
elements) oxides and ion-irradiation effects**

A Thesis Submitted to

Indian Institute of Technology Delhi

in partial fulfillment of the requirements for the degree of

Doctor of Philosophy

in Physics

Faculty of Science

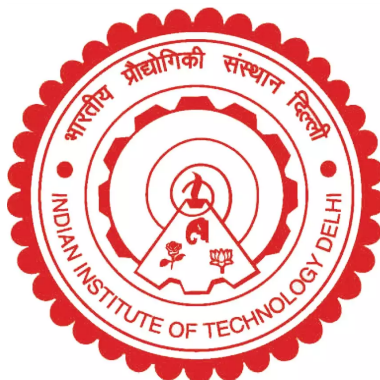
by

RAMCHARAN MEENA

(2019PHZ8034)

under the supervision of

Prof. Rajendra Singh Dhaka



Novel Materials and Interface Physics Laboratory

Department of Physics

Indian Institute of Technology Delhi (IITD)

Hauz Khas, New Delhi-110016, India

October 2024

Dedicated to

**My parents and my family for their love, care, and
affection**

DECLARATION BY THE CANDIDATE

I, **Ramcharan Meena**, hereby declare that the thesis entitled “ *Dielectric relaxation and impedance spectroscopy of NASICON type $Na_{3+x}Zr_{2-x}M_xSi_2PO_{12}$ ($M = \text{divalent, trivalent, tetravalent elements}$) oxides and ion-irradiation effects*” is my original work conducted under the supervision of Prof. Rajendra S. Dhaka and has been approved by the Student Research Committee (SRC) at the Department of Physics, Indian Institute of Technology Delhi, New Delhi, India. Furthermore, I confirm that this work has not been submitted and will not be submitted to any other institute or university for any degree or diploma. I assure compliance with the ethical code of conduct prescribed by the institute. I have duly acknowledged and credited all materials, theoretical analysis, data, figures, and text taken from other sources by appropriately citing them in the thesis. Further, I confirm that I have not used any artificial intelligence (AI) based software for writing any part of the thesis.

Signature _____

Name of the candidate: Ramcharan Meena

Entry Number: 2019PHZ8034

Department of Physics

Indian Institute of Technology Delhi

Hauz Khas, New Delhi – 110016, India.

Date:

CERTIFICATE OF THE SUPERVISOR

This is to certify that **Ramcharan Meena**'s thesis, “ *Dielectric relaxation and impedance spectroscopy of NASICON type $Na_{3+x}Zr_{2-x}M_xSi_2PO_{12}$ ($M = \text{divalent, trivalent, tetravalent elements}$) oxides and ion-irradiation effects,*” submitted to the Department of Physics, Indian Institute of Technology Delhi, for the award of the degree of **Doctor of Philosophy** in Physics, is an original record of his research work. He worked under my supervision and guidance to complete the requirements for submitting this thesis, which I feel reached an acceptable standard. He fulfilled the requirements for submitting the thesis, which, to the best of my knowledge, was of sufficient quality. The thesis results have not been submitted, in part or entirely, to any other university or institute for the award of any degree or diploma.

Signature _____

Prof. Rajendra S. Dhaka

Associate Professor

Department of Physics

Indian Institute of Technology Delhi

Hauz Khas, New Delhi – 110016, India.

Date:

ACKNOWLEDGEMENT

Foremost, I pray to the Almighty for blessing, knowledge, well-being, and unwavering strength throughout my Ph.D. expedition and the successful completion of this thesis. This Ph.D. odyssey has been a treasure trove of experiences. I acknowledge that this accomplishment would have been unattainable without my supervisor, Prof. Rajendra Singh Dhaka, for his unwavering support and invaluable guidance. I extend my heartfelt gratitude to him for affording me the incredible opportunity to work within his research group and providing the necessary research infrastructure for my endeavors. His consistent mentorship, unwavering encouragement, collaborative spirit, and insightful suggestions have been instrumental in steering me toward the successful culmination of this thesis. I extend my deepest appreciation during this journey, which presented its share of challenges and fluctuations, including agreements and disagreements, with Prof. Dhaka's steadfast dedication, discipline, and punctuality, which consistently motivated and inspired me to progress in my research work.

I am deeply thankful to the members of the Students Research Committee (SRC) Prof. Sujeet Chaudhary, Prof. Santanu Ghosh, and Prof. Pawan Kumar Kulriya for their valuable suggestions and guidance during the semester presentations. I also would like to thank my teachers who taught me during the coursework of my Ph.D. and provided insightful and meticulous knowledge of the basics of science, which helped me a lot in the research.

I acknowledge the Department of Physics at IIT Delhi for granting access to the XRD facility and Material Science division of the Inter-University Accelerator Center (IUAC) all experimental facilities used to carry out the research work presented in this thesis. I am also thankful to Pelletron group of IUAC for their support during the irradiation experiments.

I am grateful to my colleagues and labmates, both past and present, who have formed a close-knit community during this Ph.D. journey. Their contributions, discussions, suggestions, and camaraderie have been invaluable during the ups and downs of this lengthy voyage. Thanks go to my labmates at IIT Delhi: Dr. Rishabh Shukla, Dr. Ajay Kumar, Dr. Jayjit Mukherjee, Dr. Guru Dutt Gupta, Jayashree Pati, Simran Sapra, Manish Kumar Singh, Madhav, Dr. Vikas Narayan Thakur, Priyanka Yadav, Sudhanshu Gupta, Riya and Pooja. They have been colleagues and a supportive family throughout these years. Further, I am profoundly grateful to my friends, seniors, and juniors at IIT Delhi, who helped alleviate stress and provided support at various stages of my Ph.D. expedition.

I am grateful to my colleagues at Inter-University Accelerator Center (IUAC), New Delhi. First, I thank Prof. Avinash Chandra Pandey (Director IUAC) for motivating us for higher studies and providing the no objection certificate (NOC). I also thank Dr. K. Asokan and Dr. Pawan Kumar Kulriya for their unconditional support and motivation. I am grateful to my colleagues in the material science group: Dr. Ambuj Tripathi (program leader), Dr. Debdulal Kabiraj, Dr.

Fouran Singh, Dr. V. V. Siva Kumar, Dr. Saif A. Khan, Dr. Indra Sulania, Mr. Sanjay Kumar Kedia and Mr. Ambuj Mishra for their constant support throughout the journey. I would also like to thank Dr. Puneeta Tripathi, Mr. Mayur Khan, Mr. Mandeep Chahal, Ms. Shilpa, and Mr. Naveen K.R. for their help during the irradiation experiments and measurements.

I want to express my warm gratitude adequately towards my beloved family members: Ganga Dhar (grandfather), Kokli Devi (Grandmother), Kailash Chand (Father), Keshar Devi (Mother), Dilip, and Ravi. I am also thankful to my in-laws family members Shambhu Singh, Shiv Lal, Prem Devi, Phoolwati, Kavita, Ashish, Alok and Balram. Their unending love, unwavering support, and continuous encouragement have been the cornerstone of my Ph.D. journey. Finally, I am very, very thankful to my wife (Beena), Babu (Viraj), and Baby (Daxita) for their support and motivation during this journey and for providing me with their valuable time. Though many not mentioned, none is forgotten. Last but not least, I owe profound gratitude to all those close to me who contributed in numerous ways, making this journey possible.

I heartily dedicate this thesis to my beloved family.

Ramcharan Meena

ABSTRACT

In the present era of rapidly growing technology, understanding of various physical properties of materials determines the suitable candidates for various technological applications such as gas sensors, energy storage, memory applications, solar cells, superconductivity, and ionic conductors. $\text{Na}_3\text{Zr}_2\text{Si}_2\text{PO}_{12}$ is one of the important members of NASICON (**Sodium Super Ionic Conductors**) family has the chemical composition of $\text{Na}_{1+x}\text{Zr}_2\text{Si}_x\text{P}_{3-x}\text{O}_{12}$, ($0 \leq x \leq 3$). It shows the structural phase transition from monoclinic to rhombohedral phase at 160° . It shows the wide range of applications in microwave absorption, Na^+ -ion batteries, and gas sensors. Microwave heating is used in food preparation, synthesis of materials, local heating in biological samples, and the medical industry. In microwave heating, the dielectric materials absorb the energy depending on the macroscopic permittivity, which is called dielectric loss, and the dielectric permittivity decides the energy storage. Hence, studying the dielectric properties is important for energy storage. The dielectric materials are characterized by measuring the complex permittivity as a function of frequency for constant temperature and as a function of temperature at constant frequency. The dielectric measurements over a wide range of frequencies provide information about the conduction mechanism, polarization mechanism, charge carrier dynamics, and relaxation behavior. $\text{Na}_3\text{Zr}_2\text{Si}_2\text{PO}_{12}$ ($x=2$) and divalent doped NASICON shows the microwave absorption and high electric permittivity at room temperature. however, these studies are limited to room temperature or microwave regions only. Therefore, my Ph.D. thesis is focused on the temperature-dependent dielectric properties of pristine and doped NASICON ceramics. The outlines of the work carried out during this journey are briefly summarized below:

First, the broad area of NASICON materials was introduced. A detailed literature survey on crystal structure, ordering, doping, and synthesis methods is discussed. The applications of NASICON in various fields are discussed. The ion-solid interaction was discussed, and the mechanism of nuclear and electronic energy loss was discussed in detail. Finally, the motivation and objective of the thesis are discussed. In the next part, the sample preparation method, various experimental techniques, and their basic principle were discussed in detail. These techniques are used for different characterizations and analyses in our study. The Rietveld analysis and the steps involved during the analysis were discussed. The working principles of scanning electron microscope (SEM) and transmission electron microscope (TEM) are discussed. The ion irradiation using swift heavy ions (SHI) is described. Various types of electrical transport measurements, such as d.c. resistivity, capacitance-loss measurements, and impedance-phase angle measurements were explained in detail. To proceed further, $\text{Na}_3\text{Zr}_2\text{Si}_2\text{PO}_{12}$ bulk samples were prepared to find out the temperature-dependent dielectric properties of pristine NASICON ceramics. The temperature dependence of electric permittivity shows the permittivity of the

order 10^4 at 400 K. The relaxation loss peaks found for low temperatures show thermally activated relaxation. The a.c conductivity follows the universal power law, showing the change in the conduction mechanism at 360 K.

Considering the doping effects on dielectric and impedance properties, we have started with the divalent ion. Ni^{2+} ion are doped into $\text{Na}_3\text{Zr}_2\text{Si}_2\text{PO}_{12}$ at the Zr site to improve its dielectric properties. The analysis shows a similar magnitude for electric permittivity up to $x=0.15$. The relaxation analysis shows a similar type of relaxation for all doped samples. The impedance analysis shows the grain and grain boundary relaxation following the thermally activated relaxation as confirmed by a.c. conductivity analysis. The modulus analysis confirms a similar type of relaxation independent of temperature. In the next part of doping, trivalent (Pr^{3+}) ions are doped at the Zr site in $\text{Na}_3\text{Zr}_2\text{Si}_2\text{PO}_{12}$ bulk samples. The larger ionic radii of Pr ions show structural distortions with increasing doping. The permittivity increases by an order of magnitude for all doped samples, showing double relaxation peaks with different activation energies. The Nyquist analysis shows the obtained ionic conductivity of the order 10^{-4} S/cm. The temperature dependence of ac conductivity and related conduction mechanism were investigated using modified power law. In the last part of doping isovalent (Ti) substitutional effects on physical properties of $\text{Na}_3\text{Zr}_2\text{Si}_2\text{PO}_{12}$ were studied. The temperature-dependent conductivity measurements show the indication of structural phase transformation. The electric permittivity increases with doping reaches of the order 10^7 for 420K. The relaxation mechanism was determined using the non-Debye relaxation models. The impedance analysis is performed using the Z-CPE model. Conductivity analysis using modified power law was performed to determine the conduction mechanism, shows the transformation of the conduction mechanism around 350 K.

The radiation stability of NASICON ceramic was checked using the Au, Ag (100 MeV), and O (90 MeV) irradiation in the fluence range of $5\text{E}11$ to $5\text{E}13$ ions/cm². The irradiated samples characterization using XRD measurements shows the amorphized type nature heavy ions such as (Au and Ag), while no structural effects were found for O irradiations. Similar types of results were obtained using microscopic TEM analyses. The obtained experimental results were explained using the dominating electronic energy loss mechanism. The last chapter discusses a brief conclusion of this thesis and the possibility of future scopes in this area.

Overall, a systematic investigation of pristine ($\text{Na}_3\text{Zr}_2\text{Si}_2\text{PO}_{12}$) and divalent (Ni^{2+}), trivalent (Pr^{3+}) and isovalent (Ti^{4+}) investigations were performed. The radiation stability of NASICON ceramics was checked using swift heavy ions. These studies are useful for finding a suitable candidate for solid oxide fuel cells, charge storage, memory devices, and gas sensors.

सारांश

तेजी से बढ़ती प्रौद्योगिकी के वर्तमान युग में, पदार्थ के विभिन्न भौतिक गुणों की समझ विभिन्न तकनीकी अनुप्रयोगों जैसे गैस संवेदक, ऊर्जा भंडार, स्मृति भंडार उपकरण, सौर सेल, अतिचालकता और आयनिक चालक के लिए उपयुक्त उम्मीदवारों को निर्धारित करती है। $\text{Na}_3\text{Zr}_2\text{Si}_2\text{PO}_{12}$ (नासिकॉन) सोडियम आधारित आयनिक अति चालक परिवार के महत्वपूर्ण सदस्यों में से एक है, जिसकी रासायनिक संरचना $\text{Na}_{1+x}\text{Zr}_2\text{Si}_x\text{P}_{3-x}\text{O}_{12}$, ($0 \leq x \leq 3$) है। यह 160°C पर एकनताक्ष से त्रिसमनताक्ष संरचनात्मक अवस्था में परिवर्तन को दर्शाता है। यह सूक्ष्मतरंग अवशोषण, Na^+ -आयन बैटरी और गैस संवेदक में अनुप्रयोगों की विस्तृत श्रृंखला को दर्शाता है। सूक्ष्मतरंग तापन का उपयोग भोजन तैयार करने, सामग्रियों के संश्लेषण, जैविक नमूनों और चिकित्सा उद्योग में किया जाता है। सूक्ष्मतरंग तापन में, परावैद्युत पदार्थ पारगम्यता के काल्पनिक भाग के आधार पर ऊर्जा को अवशोषित करते हैं, जिसे परावैद्युत हानि कहा जाता है, और पारगम्यता का वास्तविक भाग ऊर्जा भंडारण का निर्णय करती है। इसलिए, ऊर्जा भंडारण के लिए परावैद्युत गुणों का अध्ययन महत्वपूर्ण है। परावैद्युत पदार्थों की विशेषता सम्मिश्र पारगम्यता को स्थिर तापमान के लिए आवृत्ति के फलन के रूप में तथा स्थिर आवृत्ति पर तापमान के फलन के रूप में मापकर निर्धारित की जाती है। आवृत्तियों की एक विस्तृत श्रृंखला पर परावैद्युत माप चालन तंत्र, ध्रुवीकरण तंत्र, आवेश वाहक गतिशीलता और विश्रान्ति के बारे में जानकारी प्रदान करते हैं। $\text{Na}_3\text{Zr}_2\text{Si}_2\text{PO}_{12}$ ($x=2$) और द्विसंयोजी मिश्रित नासिकॉन कमरे के तापमान पर सूक्ष्मतरंग अवशोषण और उच्च विद्युत पारगम्यता दर्शाता है, हालाँकि, ये अध्ययन केवल कमरे के तापमान या सूक्ष्मतरंग क्षेत्रों तक ही सीमित हैं, इसलिए, मेरा शोध प्रबंध असली और मिश्रित नासिकॉन सिरैमिक्स के तापमान पर निर्भर परावैद्युत गुणों पर केंद्रित है। इस दौरान किए गए कार्यों की रूपरेखा संक्षेप में नीचे दी गई है:

सर्वप्रथम नासिकॉन पदार्थ के व्यापक क्षेत्र को पेश किया गया है। क्रिस्टल संरचना, क्रमीकरण, मिश्रित और संश्लेषण विधियों पर विस्तृत साहित्य सर्वेक्षण के साथ विभिन्न क्षेत्रों में नासिकॉन के अनुप्रयोगों पर चर्चा की गई है। आयन-टोस पारस्परिक प्रभाव पर तथा नाभिकीय और इलेक्ट्रॉनिक ऊर्जा हानि के तंत्र पर विस्तार से चर्चा की गई है। अंत में, थीसिस की प्रेरणा और उद्देश्य पर चर्चा की गई है। अगले भाग में नमूना तैयार करने की विधि, विभिन्न प्रयोगात्मक तकनीकों और उनके मूल सिद्धांतों पर विस्तार से चर्चा की गई है। हमारे अध्ययन में विभिन्न लक्षण-वर्णन और विश्लेषण के लिए इन तकनीकों का उपयोग किया गया है। रीटवेल्ड विश्लेषण और विश्लेषण के दौरान शामिल चरणों पर चर्चा की गई है। सूक्ष्म दर्शन इलेक्ट्रॉन सूक्ष्मदर्शी (एसईएम) और पारदर्शी संचरण इलेक्ट्रॉन सूक्ष्मदर्शी (टीईएम) के कार्य सिद्धांतों पर चर्चा की गई है। तीव्र भारी आयनों (एसएचआई) का उपयोग करके आयन किरणन का वर्णन किया गया है। विभिन्न प्रकार के विद्युत परिवहन माप, जैसे डी.सी. प्रतिरोधकता, धारिता-परावैद्युत हानि तथा प्रतिबाधा-कला कोण माप को विस्तार से समझाया गया है। इसके बाद नासिकॉन सिरैमिक के तापमान पर निर्भर परावैद्युत गुणों का पता लगाने के लिए के थोक नमूने तैयार किए गए। विद्युत पारगम्यता की तापमान निर्भरता 400 K पर 10^4 क्रम की पारगम्यता दर्शाती है। निम्न तापमानों पर पाए गए परावैद्युत हानि प्रभाव, ऊष्मीय रूप से सक्रिय

विश्रांति को दर्शाते हैं। प्रत्यावर्ती धारा चालकता सार्वभौमिक शक्ति नियम का अनुसरण करती है, जो 360 K पर चालन तंत्र में परिवर्तन दर्शाती है।

परावैद्युत और प्रतिबाधा गुणों पर मिश्रण प्रभाव का अध्ययन के लिए, हमने द्विसंयोजी आयन से शुरुआत की है। इसके परावैद्युत गुणों में सुधार करने के लिए Ni^{2+} आयन को Zr स्थल पर नासिकॉन में अपमिश्रित किया गया है। विश्लेषण से पता चलता है कि $x=0.15$ तक विद्युत पारगम्यता के लिए समान परिमाण है। विश्राम विश्लेषण सभी मिश्रित किये गए नमूनों के लिए एक समान प्रकार का विश्रांति दर्शाता है। प्रतिबाधा विश्लेषण, तापीय रूप से सक्रिय कण और कण सीमा शिथिलन को दर्शाता है, जैसा कि प्रत्यावर्ती धारा चालकता विश्लेषण द्वारा पुष्टि की गई है। मापांक विश्लेषण तापमान से स्वतंत्र एक समान प्रकार की विश्राम अवस्था की पुष्टि करता है। मिश्रण के अगले भाग में, त्रिसंयोजक (Pr^{3+}) आयनों को नासिकॉन में Zr स्थल पर अपमिश्रित किया गया है। Pr आयनों की बड़ी आयनिक त्रिज्या बढ़ती डोपिंग के साथ संरचनात्मक विकृतियाँ दिखाती है। सभी मिश्रित किए गए नमूनों के लिए विद्युतशीलता (पारगम्यता) एक परिमाण के क्रम से बढ़ जाती है, जो विभिन्न सक्रियण ऊर्जाओं के साथ दोहरे विश्राम शिखरों को दर्शाती है। नाइकिस्ट विश्लेषण से 10^{-4} सीमेंस./सेमी के क्रम की आयनिक चालकता प्राप्त होती है। संशोधित शक्ति कानून का उपयोग करके एसी चालकता और संबंधित चालन तंत्र की तापमान निर्भरता की जांच की गई। मिश्रण के अंतिम भाग में नासिकॉन के भौतिक गुणों पर समसंयोजी (Ti) प्रतिस्थापन प्रभावों का अध्ययन किया गया। तापमान पर निर्भर चालकता माप संरचनात्मक परिवर्तन का संकेत देते हैं। मिश्रण के साथ विद्युत विद्युतशीलता (पारगम्यता) 420 K पर 10^7 क्रम के परिमाण में जाती है। विश्रांति प्रकार का निर्धारण गैर-डेबाई विश्रांति मॉडल का उपयोग करके किया गया। प्रतिबाधा विश्लेषण प्रतिबाधा-स्थिर चरण तत्व मॉडल का उपयोग करके किया जाता है। चालन तंत्र निर्धारित करने के लिए संशोधित शक्ति कानून का उपयोग करके चालकता विश्लेषण किया गया, जो 350 K के आसपास चालन तंत्र के परिवर्तन को दर्शाता है।

नासिकॉन सिरेमिक की विकिरण स्थिरता की जाँच 5E11 से 5E13 आयन/सेमी² की प्रवाह सीमा में Au, Ag (100 MeV) और O (90 MeV) विकिरण का उपयोग करके की गई। एक्स-रे विवर्तन माप का उपयोग करके विकिरणित नमूनों के लक्षण वर्णन में भारी आयनों जैसे (Au और Ag) के लिए अव्यवस्थित संरचना, जबकि O विकिरणों के लिए कोई संरचनात्मक प्रभाव नहीं पाया गया। पारदर्शी संचरण इलेक्ट्रॉन सूक्ष्मदर्शी (टीईएम) विश्लेषण का उपयोग करके इसी प्रकार के परिणाम प्राप्त किये गये। प्राप्त प्रयोगात्मक परिणामों को प्रमुख इलेक्ट्रॉनिक ऊर्जा हानि तंत्र का उपयोग करके समझाया गया है। अंतिम अध्याय में इस थीसिस का संक्षिप्त निष्कर्ष तथा इस क्षेत्र में भविष्य की संभावनाओं पर चर्चा की गई है।

कुल मिलाकर, मुल नासिकॉन और द्विसंयोजी (Ni^{2+}), त्रिसंयोजी (Pr^{3+}) और समसंयोजी (Ti^{4+}) मिश्रित नासिकॉन का एक व्यवस्थित अध्ययन किया गया है। तेज भारी आयनों का उपयोग करके नासिकॉन सिरेमिक की विकिरण स्थिरता की जाँच की गई। ये अध्ययन आवेश भंडारण, ठोस ऑक्साइड ईंधन सेल, स्मृति भंडारण, गैस संवेदक और विकिरण वातावरण के लिए उपयोगी हैं।

Contents

Declaration by the Candidate	ii
Certificate of the Supervisor	iii
Acknowledgement	iv
Abstract	vi
List of Figures	xiii
List of Tables	xxii
1 Introduction	1
1.1 Historical and Deciphering Background	1
1.2 Literature Survey	6
1.2.1 Synthesis method	7
1.2.2 Aliovalent doping	9
1.2.2.1 Doping with divalent and trivalent atoms	9
1.2.2.2 Doping with isovalent and pentavalent atoms	10
1.3 Applications of NASICON	11
1.3.1 Microwave absorption materials	11
1.3.2 All solid-state Na ion batteries	11
1.3.3 Gas sensors	11
1.4 Ion-solid Interaction	12
1.4.1 Nuclear energy loss(S_n): Low energy implanation or irradiation	13
1.4.2 Electronic energy loss(S_e): Swift heavy ion irradiation	14
1.5 Motivation of the Thesis	16
1.6 Objectives of the Thesis	17
1.7 Organization of Thesis Chapters	17
Bibliography	22
2 Experimental Details	28
2.1 Sample preparation	29
2.2 Swift heavy ion (SHI) irradiation	30

2.2.1	SNICS ion source	31
2.2.2	Pelletron accelerator	31
2.2.3	Material science beamline	32
2.3	Characterization Techniques	33
2.3.1	X-Ray Diffraction	33
2.3.2	Rietveld Refinement Method	35
2.4	Scanning Electron Microscopy (SEM)	36
2.4.1	Working principle of SEM	37
2.5	Energy Dispersive X-Ray Spectroscopy	38
2.5.1	Working principle of EDX	39
2.6	Transmission Electron Microscopy (TEM)	40
2.6.1	Working principle of TEM	40
2.7	Electrical-transport measurments	42
2.7.1	Resistivity measurments:	43
2.7.1.1	Constant current method:	43
2.7.1.2	Constant voltage method:	44
2.7.2	Dielectric measurments:	45
2.7.2.1	Dielectric mechanisms:	46
2.7.2.2	Orientalional or dipolar polarization:	47
2.7.2.3	Electronic or atomic polarization:	48
2.7.2.4	Interfacial or space charge polarization:	48
2.7.2.5	Relaxation time:	48
2.7.3	Dielectric and impedance measurements:	50
2.7.3.1	Auto-Balancing Bridge Method:	50
	Bibliography	53
3	Dielectric properties and impedance spectroscopy of NASICON type $\text{Na}_3\text{Zr}_2\text{Si}_2\text{PO}_{12}$	56
3.1	Introduction	57
3.2	Experimental Details	58
3.3	Results and Discussion	59
3.4	Conclusions	73
	Bibliography	75
4	Temperature dependent conductivity, dielectric relaxation, electrical modulus and impedance spectroscopy of Ni substituted $\text{Na}_{3+2x}\text{Zr}_{2-x}\text{Ni}_x\text{Si}_2\text{PO}_{12}$	80
4.1	Introduction	81
4.2	Experimental Details	83
4.3	Results and discussion	84
4.4	Summary and Conclusions	107
	Bibliography	108
5	Structural properties, dielectric relaxation and impedance spectroscopy of NASICON type $\text{Na}_{3+x}\text{Zr}_{2-x}\text{Pr}_x\text{Si}_2\text{PO}_{12}$ ceramics.	116
5.1	Introduction	117
5.2	Experimental Details	119
5.3	Results and Discussion	120
5.4	Conclusions	143

Bibliography	144
6 Isovalent substitutional effect on structural and electrical transport properties of NASICON type ($\text{Na}_3\text{Zr}_{2-x}\text{Ti}_x\text{Si}_2\text{PO}_{12}$) ($x=0.1-0.4$) ceramics.	151
6.1 Introduction	152
6.2 Experimental	154
6.3 Results and discussion	155
6.4 Conclusion	176
Bibliography	177
7 Structural and microscopic studies of ion-irradiated NASICON ($\text{Na}_3\text{Zr}_2\text{Si}_2\text{PO}_{12}$) ceramics.	183
7.1 Introduction	184
7.2 Experimental	185
7.3 Results and Discussion	188
7.4 Conclusion	197
Bibliography	198
8 Overall summary and Future Scope of the Work	201
9 Appendix	205
Publications	210
Conferences/Schools and Presentations	210
Biodata	212

List of Figures

1.1	Schematic representation of ion conduction path in (a) rhombohedral and (b) monoclinic phase. The arrows in the rhombohedral phase [figure (a)] represent the $\text{Na}_1\text{-Na}_2\text{-Na}_1$ single path for hopping and monoclinic phase [figure (b)] shows the two different $\text{Na}_1\text{-Na}_2\text{-Na}_1$ and $\text{Na}_1\text{-Na}_3\text{-Na}_1$ paths available for hopping. The figure is taken from reference [7].	2
1.2	Schematic representation of grain or bulk and grain boundary contribution at a particular temperature. Here, R_b is the grain or bulk resistance, R_{gb} is the grain boundary resistance, and R is the total resistance. The figure is taken from reference [5].	3
1.3	(a) X-ray diffraction pattern of $\text{Na}_3\text{Zr}_2\text{Si}_2\text{PO}_{12}$ at various selected temperatures shows the monoclinic to rhombohedral phase transition. (b) shows the enlarged view of the XRD peaks representing the gradual transformation of XRD peaks from nonsymmetric (monoclinic phase) to symmetric (rhombohedral phase) structure. The figure is taken from reference [14].	5
1.4	Figure showing the bond length variations of the NASICON phase in the monoclinic and rhombohedral phases. The figure is taken from reference [20].	6
1.5	The temperature-dependent conductivity comparison of various sample preparation method for $\text{Na}_3\text{Zr}_2\text{Si}_2\text{PO}_{12}$. The figure is taken from reference [5].	8
1.6	Electronic (S_e) and nuclear energy (S_n) loss for $\text{Na}_3\text{Zr}_2\text{Si}_2\text{PO}_{12}$ at various energies.	13
1.7	Schematic diagram explaining the track formation in thermal spike model. The figure is taken from reference [66].	15
1.8	(a) Dielectric constant and (b) loss variations with frequency for $\text{Na}_3\text{Zr}_2\text{Si}_2\text{PO}_{12}$ samples. The figure is taken from reference [36].	16
2.1	Schematic of Pelletron accelerator available at Inter-University Accelerator Center (IUAC), New Delhi, India.	32
2.2	A schematic representation of X-ray diffraction using Bargg's law.	34
2.3	(a) Schematic diagram of the scanning electron microscopy (SEM) explaining the working principle [18], and (b) Real photograph of SEM set-up used in the characterization at IUAC, New Delhi.	36
2.4	The schematic diagram of various processes occurs due to electron beam sample interaction.	37
2.5	The schematic diagram of the semiconductor detector used for the energy-dispersive X-ray spectroscopy (EDX) measurement.	39
2.6	(a) Schematic diagram of the transmission electron microscopy (TEM) explaining the working principle [24], and (b) Real photograph of TEM set-up used in the characterization at IUAC, New Delhi.	41
2.7	The schematic diagram of the resistivity measurement using the constant current method in (a) two-probe mode or (b) four-probe mode.	43

2.8	The schematic diagram of the resistivity measurement using the constant voltage source method.	44
2.9	(a) The parallel plate capacitor geometry shows vacuum capacitance due to free space. (b) Once the dielectric is inserted into the plates, external current flows in the circuit, showing that more charge is stored on electrodes. (c) Increase in capacitance due to insertion of dielectric material [32].	45
2.10	Parallel plate configuration when an alternating voltage is applied across the materials.	46
2.11	Dielectric mechanism response under the applied frequency. The figure is taken from reference [33].	47
2.12	Schematic diagram of auto-balance bridge method [33].	50
2.13	Schematic diagram of the dielectric and impedance spectroscopy measurement.	52
3.1	(a) The room temperature XRD pattern (red circle) of $\text{Na}_3\text{Zr}_2\text{Si}_2\text{PO}_{12}$ sample. The solid black line shows the Rietveld refinement profile; green and pink short verticals show the Bragg peak positions for $\text{Na}_3\text{Zr}_2\text{Si}_2\text{PO}_{12}$ sample and small impurity of ZrO_2 , and the blue line shows the residual. (b) The electrical resistivity in the temperature range of 270–400 K. The inset shows $\ln(\rho_T)$ vs. $(1000/T)$ plot, where the solid line represents the linear fit of the Arrhenius thermal conduction model.	59
3.2	(a) The current-voltage (I-V) curves (shown in linear scale), (b) the log I–log V plot, and (c) linear extrapolation of the log-log plot for I-V curves of the $\text{Na}_3\text{Zr}_2\text{Si}_2\text{PO}_{12}$ sample at the selected temperatures. The vertical dashed line in (b) represents the characteristic voltage of SCLC conduction.	61
3.3	(a) The dielectric constant and (b) loss tangent as a function of temperature for $\text{Na}_3\text{Zr}_2\text{Si}_2\text{PO}_{12}$ sample at different selected frequencies. The arrow in (a) shows the dielectric relaxation behavior and shows the corresponding relaxation peak in (c) shifts towards high temperature with an increased frequency. (d) shows the Arrhenius plot ($\ln(\tau)$ vs. $1000/T$) of relaxation time to find the activation energy of dipole relaxation.	63
3.4	The real (a) and imaginary (b) parts of dielectric constant as a function of frequency (20 Hz–2 MHz) at different temperatures (200–400 K) for the $\text{Na}_3\text{Zr}_2\text{Si}_2\text{PO}_{12}$ sample.	64
3.5	The real (a) and imaginary (b) parts of impedance as a function of frequency (20 Hz–2 MHz) at different temperatures (200–400 K) for the $\text{Na}_3\text{Zr}_2\text{Si}_2\text{PO}_{12}$ sample. Figure (c) and (d) shows the same data but in a log scale for clarity.	65
3.6	(a) The frequency dependence of <i>a.c.</i> conductivity for the $\text{Na}_3\text{Zr}_2\text{Si}_2\text{PO}_{12}$ sample at various temperatures, and (b) the temperature dependence of <i>s</i> parameter on the left scale and $(1-s)$ on the right scale. The open symbols represent the experimental data, and the solid line represents the fit. The dashed line in (b) around 365 K separates the CBH and the NSPT conduction regions.	67
3.7	The variation of hopping distances (a, c), and effective density of states (b, d) with frequency at different temperatures for the $\text{Na}_3\text{Zr}_2\text{Si}_2\text{PO}_{12}$ sample in CBH and NSPT regions, respectively.	69
3.8	The plot between $\ln(\sigma_{ac}^*T)$ vs. $(1000/T)$ for the $\text{Na}_3\text{Zr}_2\text{Si}_2\text{PO}_{12}$ sample at selected frequencies, open symbols and solid lines show the experimental data and linear fit, respectively. The dashed line separates the regions of two different types of conduction mechanisms following NSPT and CBH models, respectively.	70

3.9	The real (a) and imaginary (b) parts of the electric modulus as a function of angular frequency at various temperatures for the $\text{Na}_3\text{Zr}_2\text{Si}_2\text{PO}_{12}$ sample. The Arrhenius plot of $\ln(\omega_m)$ versus $1000/T$ is shown (c).	71
3.10	(a) Scaling behavior of imaginary part of electric modulus M'' versus angular frequency ω at various temperature. (b) The combined impedance and electric modulus spectrum of $\text{Na}_3\text{Zr}_2\text{Si}_2\text{PO}_{12}$ sample at room temperature.	73
4.1	(a–d) The Rietveld refined room temperature x-ray diffraction (XRD) patterns of (a) $\text{Na}_{3.1}\text{Zr}_{1.95}\text{Ni}_{0.05}\text{Si}_2\text{PO}_{12}$, (b) $\text{Na}_{3.2}\text{Zr}_{1.9}\text{Ni}_{0.1}\text{Si}_2\text{PO}_{12}$, (c) $\text{Na}_{3.3}\text{Zr}_{1.85}\text{Ni}_{0.15}\text{Si}_2\text{PO}_{12}$, and (d) $\text{Na}_{3.4}\text{Zr}_{1.8}\text{Ni}_{0.2}\text{Si}_2\text{PO}_{12}$ samples. The observed, calculated, and the difference between observed and calculated patterns are shown by the open red circle, black solid line, and continuous blue line, respectively; green, violet, and brown vertical markers represent the Bragg positions corresponding of the C 2/c, P 1 21/c and P -4 21 c space groups, respectively.	85
4.2	The combined XRD plot of all the Ni-doped NASICON samples in the Y-offset scheme. The *-symbol shows the impurity due to ZrO_2 phase and # symbols shows the Na_3PO_4 impurity phase.	87
4.3	The scanning electron microscope (SEM) images (a–d) of $\text{Na}_{3+2x}\text{Zr}_{2-x}\text{Ni}_x\text{Si}_2\text{PO}_{12}$ ($x=0.05-0.2$) samples showing the non-uniform distribution of particles. All the images are taken at a similar scale at the bottom of each panel. The particle size distribution is shown in the inset of each panel, where the vertical bars show the number of particles and the red solid line shows the fitting using the Gaussian function.	88
4.4	Energy dispersive X-ray spectrum of $\text{Na}_{3+2x}\text{Zr}_{2-x}\text{Ni}_x\text{Si}_2\text{PO}_{12}$ ($x = 0.05-0.2$) samples. The various X-ray peaks in the spectrum are labeled with corresponding elements. The spectra show the absence of unwanted additional elemental peaks.	89
4.5	The temperature dependent resistivity variation of the $\text{Na}_{3+2x}\text{Zr}_{2-x}\text{Ni}_x\text{Si}_2\text{PO}_{12}$ ($x=0.05-0.2$) samples in panels (a–d). The inset in each panel shows the Arrhenius thermal conduction using the plot of $(\ln \rho$ versus $1000/T)$ to find the activation energy of thermal conduction. Here, the open circles represent the experimental data and the solid line represents the linear fit.	90
4.6	The temperature-dependent dielectric constant variation of the $\text{Na}_{3+2x}\text{Zr}_{2-x}\text{Ni}_x\text{Si}_2\text{PO}_{12}$ ($x = 0.05-0.2$) samples at different selected frequencies, as shown in panels (a–d). The arrows in each panel show the shifting of the relaxation peak toward the high-temperature side with an increase in the frequency.	91
4.7	The temperature-dependent dielectric loss variation of $\text{Na}_{3+2x}\text{Zr}_{2-x}\text{Ni}_x\text{Si}_2\text{PO}_{12}$ ($x=0.05-0.2$) samples at various selected frequencies, are shown in panels (a–d). The loss peak shifts toward the high-temperature side with an increase in frequency. The inset in each panel shows the plot of $(\ln \tau$ versus $1000/T)$, where the open circle represents the experimental data and the solid lines show the Arrhenius fit.	92
4.8	The temperature-dependent real part of dielectric permittivity of $\text{Na}_{3+2x}\text{Zr}_{2-x}\text{Ni}_x\text{Si}_2\text{PO}_{12}$ ($x = 0.05-0.2$) samples as a function of frequency, as shown in panels (a–d). The arrows indicate an increase in relaxation frequency towards the high-temperature side with an increase in temperature from 140–400 K. The real permittivity data are fitted using modified Cole-Cole equation 5(a), shown as solid lines in each panel.	94

4.9	The temperature-dependent imaginary part of dielectric permittivity $\text{Na}_{3+2x}\text{Zr}_{2-x}\text{Ni}_x\text{Si}_2\text{PO}_{12}$ ($x = 0.05-0.2$) samples as a function of frequency are shown in figure (a-d). The arrow shows an increase in relaxation frequency towards the high-temperature side with an increase in temperature from 140–400 K. The imaginary permittivity data are fitted using modified Cole-Cole equation 5(b), shown as solid lines in each panel.	95
4.10	The frequency dependence of real impedance data for the $\text{Na}_{3+2x}\text{Zr}_{2-x}\text{Ni}_x\text{Si}_2\text{PO}_{12}$ ($x=0.05-0.2$) samples at various selected temperatures are shown in panels (a–d). The two arrows in these panels show the relaxation due to grain-boundary (at lower frequencies side) and grains (at higher frequency side). The arrow directions show an increase in relaxation towards the high-frequency side with an increase in temperature.	96
4.11	The imaginary part of total impedance for the $\text{Na}_{3+2x}\text{Zr}_{2-x}\text{Ni}_x\text{Si}_2\text{PO}_{12}$ ($x=0.05-0.2$) samples at various temperatures as a function of frequency are shown in panels (a–d). The arrow shows an increase in relaxation peak towards the high-frequency side with an increase in temperature. All these curves deviate from the perfect circular arc, representing the non-Debye type relaxation behavior. . .	97
4.12	The real part of electric modulus (M') variation with frequency for the $\text{Na}_{3+2x}\text{Zr}_{2-x}\text{Ni}_x\text{Si}_2\text{PO}_{12}$ ($x=0.05-0.2$) samples in the temperature range of 140–400 K are shown in panels (a–d). Here, the dashed arrow indicates the direction in which the temperature is increasing.	98
4.13	The imaginary part of electric modulus M'' for the $\text{Na}_{3+2x}\text{Zr}_{2-x}\text{Ni}_x\text{Si}_2\text{PO}_{12}$ ($x=0.05-0.2$) samples in the temperature range of 140–200 K are shown in panels (a–d). Here, the open symbol represents the experimental data, and the solid red lines represent the fit to the KWW function. The dashed black arrows in each panel indicate the direction of the relaxation peak shift with increasing temperature.	99
4.14	The imaginary part of electric modulus M'' for the $\text{Na}_{3+2x}\text{Zr}_{2-x}\text{Ni}_x\text{Si}_2\text{PO}_{12}$ ($x=0.05-0.2$) samples in the temperature range of 220–400 K are shown in panels (a–d). Here, the dashed arrows indicate the increase in relaxation frequency with increased sample temperature.	100
4.15	The Arrhenius activation energy of relaxation for the $\text{Na}_{3+2x}\text{Zr}_{2-x}\text{Ni}_x\text{Si}_2\text{PO}_{12}$ ($x=0.05-0.2$) samples, shown in panels (a–d) at room temperature. Here, the open symbols represent the experimental data and the dashed lines represent the linear fit to equation 7.	101
4.16	The scaling analysis of imaginary electric modulus of $\text{Na}_{3+2x}\text{Zr}_{2-x}\text{Ni}_x\text{Si}_2\text{PO}_{12}$ ($x=0.05-0.2$) samples at various temperatures are shown in figure (a-d). In all these figures, the open symbol represents the experimental data, and the arrow shows the increase in temperature. The merging of all these curves into a single master curve shows a similar type of relaxation.	103
4.17	The <i>a.c.</i> conductivity variation of $\text{Na}_{3+2x}\text{Zr}_{2-x}\text{Ni}_x\text{Si}_2\text{PO}_{12}$ ($x=0.05-0.2$) samples at various temperatures are shown in figure (a-d). In all the figures the open symbol represents the experimental data and the solid line represents the fit using the double power law equation 13.	104
4.18	The temperature dependence of the Power law exponents m , n for the $\text{Na}_{3+2x}\text{Zr}_{2-x}\text{Ni}_x\text{Si}_2\text{PO}_{12}$ ($x = 0.05-0.2$) samples above room temperature are shown in panels (a) and (b). These exponents increase with temperature, showing the small polaron type hopping conduction in these samples.	106

5.1	The schematic representation of $\text{Na}_3\text{Zr}_2\text{Si}_2\text{PO}_{12}$ in monoclinic structure (C 2/c phase), which shows the ZrO_6 octahedra (light brown) and Si/PO_4 tetrahedra (pink color) along with three types of Na sites per unit cell. The arrows show the conduction path along $\text{Na}_2/\text{Na}_3\text{-Na}_1\text{-Na}_2/\text{Na}_3$ sites.	118
5.2	Reitveld refinement spectra of Pr-doped NASICON samples having the compositions of $\text{Na}_{3+x}\text{Zr}_{2-x}\text{Pr}_x\text{Si}_2\text{PO}_{12}$ ($x=0.05\text{-}0.2$) are shown in (a-d). Here, open red symbols represent experimental data, and solid black line shows the Rietveld refined XRD patterns. The Bragg's positions correspond to the monoclinic NASICON phase is shown by green vertical lines, and Bragg's peak corresponds to ZrO_2 and $\text{Na}_3\text{Pr}(\text{PO}_4)_3$ impurity phases are marked by * and # symbols are shown as verticles lines of violet and wine color respectively. The blue color solid line represents the difference between observed and calculated data.	121
5.3	(a) Lattice parameters of Pr-doped NASICON samples obtained after the refinement and (b) show the Distortion in a-base and shear deformation in unit cell as a function of Pr-doping concentration.	122
5.4	(a-d) shows microstructural images of $\text{Na}_{3+x}\text{Zr}_{2-x}\text{Pr}_x\text{Si}_2\text{PO}_{12}$ ($x=0.05\text{-}0.2$) samples obtained using field emission scanning electron microscope (FESEM). These images are taken at an acceleration voltage of 25 kV at a magnification of $5\mu\text{m}$. (e-h) shows the energy dispersive X-ray data of $\text{Na}_{3+x}\text{Zr}_{2-x}\text{Pr}_x\text{Si}_2\text{PO}_{12}$ ($x = 0.05\text{-}0.2$) samples. The various X-ray peaks in the data are labeled with corresponding elements. The spectra show the absence of unwanted elemental peaks	124
5.5	The temperature-dependent variations in dielectric constant (ϵ_r) (a-d) of $\text{Na}_{3+x}\text{Zr}_{2-x}\text{Pr}_x\text{Si}_2\text{PO}_{12}$ ($x = 0.05\text{-}0.2$) samples at various selected frequencies from 100 Hz to 2 MHz. The arrows in panel (a) show the shifting of the relaxation peak toward the high-temperature side with an increase in the frequency.	125
5.6	The temperature-dependent variations in loss tangent ($\tan\delta$) (a-d) of $\text{Na}_{3+x}\text{Zr}_{2-x}\text{Pr}_x\text{Si}_2\text{PO}_{12}$ ($x = 0.05\text{-}0.2$) samples at various selected frequencies from 100 Hz to 2 MHz. The arrows in panel (a) show the shifting of the relaxation peak toward the high-temperature side with an increase in the frequency.	126
5.7	The temperature dependence of relaxation time for peak 1 in (a) in the low-temperature range and for peak 2 in (b) at high temperatures. The open symbols show the measured data points and the solid lines show the linear fit.	127
5.8	Isothermal frequency dependent real permittivity for $\text{Na}_{3+x}\text{Zr}_{2-x}\text{Pr}_x\text{Si}_2\text{PO}_{12}$ ($x=0.05\text{-}0.2$) samples at various selected temperature. Here, open symbols are measured experimental data, and the solid line is fitting using the modified Cole-Cole relaxation, including the contributions from complex electrical conductivity.	128
5.9	Isothermal frequency dependent imaginary part of electric permittivity (ϵ'') variations with frequency at selected temperatures of $\text{Na}_{3+x}\text{Zr}_{2-x}\text{Pr}_x\text{Si}_2\text{PO}_{12}$ ($x=0.05\text{-}0.2$) samples. Here, the open symbols show the measured experimental data, and the solid line is the fitting using modified Cole-Cole relaxation.	129
5.10	The real (Z') part of total impedance are shown in figure (a-d) as a function of frequency for $\text{Na}_{3+x}\text{Zr}_{2-x}\text{Pr}_x\text{Si}_2\text{PO}_{12}$ ($x=0.05\text{-}0.2$) samples at selected temperatures. The arrow indicates the direction of increasing temperature.	131
5.11	The imaginary (Z'') part of total impedance are shown in figure (a-d) as a function of frequency for $\text{Na}_{3+x}\text{Zr}_{2-x}\text{Pr}_x\text{Si}_2\text{PO}_{12}$ ($x=0.05\text{-}0.2$) samples at selected temperatures. The arrow indicates the direction of increasing temperature.	132

5.12	The Nyquist plot of Pr-doped NASICON ceramics at selected temperatures. Here, the open symbols show the experimental data and the solid lines fit using the equivalent circuit model. The deviation at lower temperatures is due to the highly insulating nature of Pr-doped samples. The fitting is performed using the ZSimpWin software.	133
5.13	The temperature-dependent total ionic conductivity of all Pr-doped NASICON ceramics.	135
5.14	The variation of real (M') (a-d) and imaginary (M'') (e-f) part of the electric modulus function at selected temperature as a function of frequency. Here, open symbols represent the measured experimental data, and a solid line is fit using the electric modulus function. The (M') and (M'') above 200K are shown in figure 9.4 and 9.5 of appendix section.	136
5.15	Arrhenius plot of peak modulus frequency with temperature for Pr-doped NASICON samples. Open symbols represent the measured peak relaxation frequency, and the solid line represents the Arrhenius linear fit.	138
5.16	The scaling analysis spectra of imaginary modulus (M'') for Pr-doped NASICON samples.	139
5.17	The frequency dependence of a.c. conductivity at selected temperatures for Pr-doped samples. Here, the open symbol represents the measured experimental data, and open red solid line shows the fit using the modified power law.	140
5.18	The temperature dependence of s parameter obtained after fitting of a.c. conductivity data using modified power law for the $\text{Na}_{3+x}\text{Zr}_{2-x}\text{Pr}_x\text{Si}_2\text{PO}_{12}$ ($x = 0.05-0.2$) samples. The increasing s values with temperature show the correlated barrier hopping (CBH) motion in the measured temperature range.	141
5.19	The Summerfield scaling of a.c. conductivity following a single master curve for the $\text{Na}_{3+x}\text{Zr}_{2-x}\text{Pr}_x\text{Si}_2\text{PO}_{12}$ ($x = 0.05-0.2$) samples.	142
6.1	Reitveld refinement spectra of Ti-doped NASICON samples $\text{Na}_3\text{Zr}_{2-x}\text{Ti}_x\text{Si}_2\text{PO}_{12}$ ($x=0.1-0.4$) are shown in (a-d). Here, open red symbols represent observed experimental data, and solid black line represents the calculated Rietveld refined XRD patterns. Green vertical lines show the Bragg's position of the monoclinic NASICON phase, and Bragg's position corresponds to $\text{Na}_3\text{P}_3\text{O}_9$ are marked by # symbols are wine color (figure d). The blue solid line represents the difference between observed and calculated data. Figure (e-h) shows the microscopic images of $\text{Na}_3\text{Zr}_{2-x}\text{Ti}_x\text{Si}_2\text{PO}_{12}$ ($x=0.1-0.4$) samples obtained using the field emission scanning electron microscope (FESEM) by taking the acceleration voltage of 15 kV with a magnification of 5 μm	155
6.2	Energy dispersive x-ray (EDX) mapping of various elements present in the $\text{Na}_3\text{Zr}_{2-x}\text{Ti}_x\text{Si}_2\text{PO}_{12}$ ($x = 0.1 - 0.4$) NASICON samples.	157
6.3	Temperature dependent resistivity variations of $\text{Na}_3\text{Zr}_{2-x}\text{Ti}_x\text{Si}_2\text{PO}_{12}$ ($x=0.1-0.4$) samples. The inset shows the $\ln\rho$ vs ($\frac{1000}{T}$) graph; here, the open symbol represents the obtained experimental data, and the solid line shows the linear fit using the Arrhenius thermal conduction model. The circle shows the signature of structural phase transition around 420 K.	158
6.4	Temperature dependence of electric permittivity (ϵ_r) as a function of temperature at selected frequencies. The arrow shows the direction of increasing frequency and shifting of relaxation peak towards the higher frequency side.	159

6.5	The dielectric loss or tangent loss variations showing the relaxation peaks for $\text{Na}_3\text{Zr}_{2-x}\text{Ti}_x\text{Si}_2\text{PO}_{12}$ ($x=0.1-0.4$) samples at selected frequencies. The shifting of the relaxation peak towards the high-temperature side is shown using the arrow.	160
6.6	Temperature dependence of relaxation time for relaxation peaks (peak 1 and peak 2) for $\text{Na}_3\text{Zr}_{2-x}\text{Ti}_x\text{Si}_2\text{PO}_{12}$ ($x=0.1-0.4$). Peak 1 belongs to the relaxation in the low-temperature range are shown in (a), and peak 2 belongs to the high-temperature relaxation, shown in (b).	161
6.7	Frequency dependence of real part of permittivity as a function of frequency at the selected temperature for $\text{Na}_3\text{Zr}_{2-x}\text{Ti}_x\text{Si}_2\text{PO}_{12}$ ($x=0.1-0.4$) samples. The experimental data is fitted using the non-Debye type relaxation and conductivity term. Here open symbol shows the experimental data and solid line is fit using the complex conductivity term.	163
6.8	Frequency dependence of imaginary permittivity as a function of frequency at the selected temperature for $\text{Na}_3\text{Zr}_{2-x}\text{Ti}_x\text{Si}_2\text{PO}_{12}$ ($x=0.1-0.4$) samples. The experimental data is fitted by considering the non-Debye type relaxation and conductivity term. Here open symbol shows the experimental data and solid line is fit using the complex conductivity term.	164
6.9	Real impedance variations as a function of frequency at for $\text{Na}_3\text{Zr}_{2-x}\text{Ti}_x\text{Si}_2\text{PO}_{12}$ ($x=0.1-0.4$) samples at selected temperatures. Here, the open symbol represents the observed experimental data, and the solid line is fit using equation 6.8a.	166
6.10	Imaginary impedance variations as a function of frequency at for $\text{Na}_3\text{Zr}_{2-x}\text{Ti}_x\text{Si}_2\text{PO}_{12}$ ($x=0.1-0.4$) samples at selected temperatures. Here, the open symbol represents the observed experimental data, and the solid line is fit using equation 6.8b.	167
6.11	Temperature dependent variations in real (M') and imaginary modulus (M'') at selected temperatures for $\text{Na}_3\text{Zr}_{2-x}\text{Ti}_x\text{Si}_2\text{PO}_{12}$ ($x=0.1-0.4$) samples. Here, the open symbol represents the measured experimental data, and the solid line is fit using equation 6.13. The (M') and (M'') above 200 K are shown in figure 9.6 and 9.7 of appendix section.	169
6.12	Temperature dependence of modulus relaxation peak of $\text{Na}_3\text{Zr}_{2-x}\text{Ti}_x\text{Si}_2\text{PO}_{12}$ ($x=0.1-0.4$) determines the activation energy (E_M) of modulus relaxation. Here, the open symbol represents the obtained experimental data and the solid line shows the linear fit using the Arrhenius thermal activation model.	171
6.13	Scaling analysis of imaginary modulus for $\text{Na}_3\text{Zr}_{2-x}\text{Ti}_x\text{Si}_2\text{PO}_{12}$ ($x=0.1-0.4$) samples. Here, the open symbol represents the experimental data, and the arrow shows the direction of increasing temperature.	172
6.14	ac conductivity variations of $\text{Na}_3\text{Zr}_{2-x}\text{Ti}_x\text{Si}_2\text{PO}_{12}$ ($x=0.1-0.4$) samples in the temperature range of 200 K-400 K. The data has been fitted using the modified power, the open symbol represents the experimental data, and the solid line is fit using equation 6.19.	174
6.15	Temperature dependent variations of S parameter for Ti-doped samples. The variation shows two types of reasons, indicating two different conducting mechanisms over a measured temperature range.	175
7.1	Comparison of electronic and nuclear energy loss for (a) Au 100 MeV, (b) Ag 100 MeV, and (c) O 90 MeV. (d) shows the comparison of electronic energy loss for Au, Ag, and O ion beams. The dashed line in all figures corresponds to the energy (100 MeV) only.	187

7.2	Reitveld refinement spectra of pristine NASICON samples $\text{Na}_3\text{Zr}_2\text{Si}_2\text{PO}_{12}$. Here, open red symbols represent observed experimental data, and solid black line represents the calculated Rietveld refined XRD patterns. Green vertical lines show Bragg's position corresponding to the monoclinic NASICON phase, and Bragg's position corresponding to ZrO_2 is shown by the *-symbol wine color. The blue solid line represents the difference between observed and calculated data.	188
7.3	Electron diffraction pattern of $\text{Na}_3\text{Zr}_2\text{Si}_2\text{PO}_{12}$ bulk samples.(a) shows the various spots observed in pristine samples, and (b) shows the labeling of the rings, confirming the polycrystalline nature of the samples. The central bright spot corresponds to the direct transmitted beam.	190
7.4	Energy dispersive x-ray (EDX) elemental analysis for $\text{Na}_3\text{Zr}_2\text{Si}_2\text{PO}_{12}$ bulk samples. Various peaks are labeled with the corresponding elements. Green color peaks belong to K shell lines and red color peaks belong to M shell lines.	191
7.5	Elemental mapping of the $\text{Na}_3\text{Zr}_2\text{Si}_2\text{PO}_{12}$ grain. The mapping shows the uniform distribution of elements within the grain.	192
7.6	GIXRD patterns of ion irradiated NASICON ceramics are shown for (a) Au 100 MeV, (b) Ag 100 MeV, (c) O 90 MeV, and (d) comparison of irradiated samples at a fluence of $5 \text{ E}13 \text{ ions/cm}^2$. The additional peaks marked with *-symbol are due to ZrO_2 impurity.	193
7.7	Expanded view of the XRD peak around 30.8 degrees (a) for Au 100 MeV (b) Ag 100 MeV (c) O 90 MeV and (d) comparison of Au, Ag and O irradiation at the fluence of $5\text{E}13 \text{ ions/cm}^2$. The peaks in (a) and (b) are shifting towards the lower angle, showing the swelling effect on irradiation. (c) Confirms no swelling effect on O ion irradiations.	194
7.8	Lattice strain as a function of ion fluence for Au, Ag, and O irradiations. The higher strain at higher fluence is due to greater damage to the samples.	195
7.9	Microscopic imaging of (a) pristine and (b-d) samples irradiated with Au, Ag and O ions of fluence $1\text{E}13 \text{ ions/cm}^2$. All images are taken at the scale of 200 nm with an accelerating voltage of 200kV.	196
7.10	Plane view of HRTEM images of Au (a-d), Ag (e-h), and O (i-l) irradiated NASICON at ions fluence of $5\text{E}12 \text{ ions/cm}^2$ and $1\text{E}13 \text{ ions/cm}^2$. The imaging is performed on the samples deposited on the Cu grid and irradiated by mounting the grid directly on the Cu ladder. The imaging is performed at the scale of 20 nm and 10 nm for better representation.	196
9.1	The temperature dependence and activation energy of relaxation frequency for the $\text{Na}_{3+2x}\text{Zr}_{2-x}\text{Ni}_x\text{Si}_2\text{PO}_{12}$ ($x = 0.05-0.2$) samples are shown in panels (a-d) for the high-temperature region. The open symbol represents the experimental data and the solid line shows the linear fit.	206
9.2	The scaling analysis of electric modulus for the $\text{Na}_{3+2x}\text{Zr}_{2-x}\text{Ni}_x\text{Si}_2\text{PO}_{12}$ ($x = 0.05-0.2$) samples above room temperature are shown in panels (a-d). The merging below the peak frequency shows a similar type of relaxation and above a different type of relaxation.	206
9.3	The combined analysis of imaginary modulus and impedance for the $\text{Na}_{3+2x}\text{Zr}_{2-x}\text{Ni}_x\text{Si}_2\text{PO}_{12}$ ($x = 0.05-0.2$) samples at room temperature are shown in panels (a-d). The non-overlapping of modulus and impedance spectra shows the short-range mobility of charge carriers.	207

9.4	The real part of electric modulus for the $\text{Na}_{3+x}\text{Zr}_{2-x}\text{Pr}_x\text{Si}_2\text{PO}_{12}$ ($x = 0.05\text{--}0.2$) samples as a function of frequency for the temperature range of 160 K -400 K. The arrow indicates the direction of increasing temperature.	207
9.5	The imaginary part of electric modulus for the $\text{Na}_{3+x}\text{Zr}_{2-x}\text{Pr}_x\text{Si}_2\text{PO}_{12}$ ($x = 0.05\text{--}0.2$) samples as a function of frequency for the temperature range of 200–400 K. The arrow indicates the direction of increasing temperature.	208
9.6	The real part of electric modulus for the $\text{Na}_3\text{Zr}_{2-x}\text{Ti}_x\text{Si}_2\text{PO}_{12}$ ($x = 0.1 - 0.4$) samples as a function of frequency for the temperature range of 160–400 K. The arrow indicates the direction of increasing temperature.	208
9.7	The imaginary part of electric modulus for the $\text{Na}_3\text{Zr}_{2-x}\text{Ti}_x\text{Si}_2\text{PO}_{12}$ ($x = 0.1 - 0.4$) samples as a function of frequency for the temperature range of 200–400 K. The arrow indicates the direction of increasing temperature.	209

List of Tables

4.1	The room temperature structural parameters of Ni-doped NASICON type $\text{Na}_{3+2x}\text{Zr}_{2-x}\text{Ni}_x\text{Si}_2\text{PO}_{12}$ ($x = 0.05\text{--}0.2$) samples obtained from profile fittings using Rietveld refinement method.	86
4.2	The calculated activation energy of dielectric relaxation (E_{relax}) and characteristic relaxation time (τ_0) for $\text{Na}_{3+2x}\text{Zr}_{2-x}\text{Ni}_x\text{Si}_2\text{PO}_{12}$ ($x=0.05\text{--}0.2$) samples.	93
5.1	The structural parameters of the $\text{Na}_{3+x}\text{Zr}_{2-x}\text{Pr}_x\text{Si}_2\text{PO}_{12}$ ($x = 0.05\text{--}0.2$) samples obtained from profile fittings using the Rietveld refinement of x-ray diffraction patterns measured at room temperature.	123
6.1	Room temperature structural parameters of Ti-doped NASICON samples obtained from profile fittings using the Rietveld method.	156
6.2	Calculated relaxation activation energy (E_{relax}) and characteristic relaxation time (τ_0) for $\text{Na}_3\text{Zr}_{2-x}\text{Ti}_x\text{Si}_2\text{PO}_{12}$ ($x=0.1\text{--}0.4$) samples in the measured temperature range of 90 K-440 K.	162
7.1	Comparison of electronic (S_e) and nuclear energy loss (S_n) for Au, Ag (100 MeV), and O (90 MeV) ions used in this work.	186
7.2	Electron diffraction pattern labelling for $\text{Na}_3\text{Zr}_2\text{Si}_2\text{PO}_{12}$ samples.	189
9.1	The room temperature structural parameters of the $\text{Na}_{3+x}\text{Zr}_{2-x}\text{Pr}_x\text{Si}_2\text{PO}_{12}$ ($x = 0.05, 0.1, 0.15, 0.2$) samples obtained from profile fittings using the Rietveld refinement method.	205